

Adjoint-based trailing edge shape optimization of a transonic turbine vane using large eddy simulations

Chaitanya Talnikar¹ Qiqi Wang¹

¹Massachusetts Institute of Technology
November 30, 2020

Abstract

The shape of the trailing edge of a gas turbine nozzle guide vane has a significant effect on the downstream stagnation pressure loss and heat transfer over the surface of the vane. Traditionally, adjoint-based design optimization methods for turbomachinery components have used low-fidelity simulations like Reynolds averaged Navier-Stokes. To reliably capture the complex flow phenomena involved in turbulent flow over a turbine vane, high-fidelity simulations like large eddy simulation (LES) are required. In this paper, an adjoint-based trailing edge shape optimization using LES is performed to reduce pressure loss and heat transfer over the surface of the vane. The chaotic dynamics of turbulence limits the effectiveness of the adjoint method for long-time averaged objective functions computed from LES. A viscosity stabilized unsteady adjoint method is used to obtain gradients of the design objective function with reasonable accuracy. A gradient utilizing Bayesian optimization is used to robustly handle noise in the objective function and gradient evaluations. The trailing edge shape is parameterized using a linear combination of 5 convex designs. Results from the optimization, performed on the supercomputer Mira, are compared with optimal designs generated using derivative-free design optimization of the same problem.

1 INTRODUCTION

In a gas turbine engine the nozzle guide vanes are responsible for directing air onto the turbine blades. Shape design of these vanes is an important problem as it influences the amount of work that can be extracted from the gases exiting the upstream combustion chamber [1]. In particular, the downstream stagnation pressure loss is quite sensitive to the shape of the trailing edge of the vane. It can alter the boundary layer development process and move the location of the separation points on the surface of the vane [2]. Additionally, the trailing edge shape impacts the amount of heat transfer from the hot gas to the surface of

the vane. Reducing the heat transfer can significantly increase the life span of the turbine vane [3].

Adjoint-based design optimization is an optimization tool used by researchers in many computational fluid dynamics (CFD) applications for improving the performance of various fluid machinery components. It uses the adjoint method to obtain gradients of the design objective with respect to design parameters [4, 5]. Gradient-based optimization algorithms require fewer iterations to reach locally optimal designs and can scale to a larger number of design parameters than the typical derivative-free optimization algorithms used in CFD [6, 7, 8]. In the field of aerospace engineering, Jameson [9] performed an adjoint-based shape optimization of an airfoil using the steady state Euler equations and Lyu [10] performed a design optimization of a blended wing body aircraft using the Reynolds Averaged Navier-Stokes (RANS) equations. Majority of the adjoint-based design optimizations carried out in literature use low-fidelity simulations like RANS or Euler [11, 9, 10, 12]. To accurately model the complex fluid flow structures in the 3-dimensional turbine vane problem, like flow separation, turbulent boundary layer development and wake mixing, high fidelity simulations like Large Eddy Simulations (LES) are required [13, 14, 15, 16, 17, 18]. Gourdain [14] compared LES to RANS on a similar turbine vane, and found that LES predicts heat transfer with a much higher accuracy. Coupling the accuracy of LES with the performance of the current generation of supercomputers, adjoint-based design using LES is becoming a more practical option [19].

The application of the adjoint method to LES introduces certain complications. The magnitude of the adjoint solution field diverges to infinity as the LES is performed for a longer time [20, 21, 22, 23, 24, 25]. This divergence introduces a significant error in the gradient computed from the adjoint solution, especially when the design objective function is a long time-averaged quantity. The authors of this paper have proposed a fix to the problem of diverging adjoint solutions by modifying the adjoint method for unsteady compressible Navier-Stokes equations [26]. Minimal artificial viscosity is added to the equations governing the adjoint solution in regions of the flow where the magnitude of the adjoint solution is believed to be growing exponentially fast. The regions of divergence of the adjoint solution are found by performing an L_2 norm analysis of the adjoint equations. Using the modified adjoint equations, the divergence of the adjoint solutions is restricted, while maintaining a reasonable accuracy of the computed gradients.

The noise in the design objective and gradient evaluations and the prohibitive computational cost of the evaluations makes design optimization with LES a challenging task [27]. Numerous optimizations algorithms have been designed for handling noisy and expensive objective functions [28]. One of the most basic methods is the Robbins-Monro algorithm [29], which decides the next design point to evaluate by taking a variable step in the gradient direction, similar to steepest descent. The algorithm has the tendency to get stuck in local optimums and requires extensive tuning of the step parameter [30, 31]. Another optimization algorithm is SNOBFIT (Stable noisy branch and fit) [32], which belongs to the divide and conquer class of optimization algorithms. While

the algorithm is robust to noise, it cannot effectively utilize gradient information from all past evaluations. Bayesian optimization algorithms have a lot of properties that make them ideal for design optimization using LES [33, 34]. In this paper, the standard Bayesian optimization algorithm is modified to make it work better for noisy evaluations.

The adjoint-based design optimization tool, using the artificial viscosity based adjoint method and the Bayesian optimization algorithm, is applied to design the trailing edge shape of a gas turbine nozzle guide vane. The design objective is a weighted combination of the time and mass-flow averaged stagnation pressure loss coefficient downstream of the vane and the time-averaged Nusselt number over the trailing edge surface of the vane. The shape of the trailing edge is parameterized using a linear combination of 5 convex designs (convex about the chord line). This makes the dimension of the optimization problem equal to 4. The optimization is performed on the Argonne National Lab Mira supercomputer and a small-scale CPU and GPU based compute cluster. Section 2 describes the physics, numerical approximation and parameterization procedure of the trailing edge shape for the flow over the 3-dimensional turbine vane. Section 3 details the artificial viscosity based adjoint method, the modified Bayesian optimization algorithm and its application to a 2-dimensional optimization problem with the Rastigrin function as the objective function. Finally, section 4 discusses results from the adjoint-based design optimization and demonstrates a comparison between gradient-based and derivative-free Bayesian optimization. Section 5 concludes the paper and examines avenues for future research and application to new design problems.

2 Flow over turbine vane

The shape of a nozzle guide vane in a gas turbine engine plays a significant role in the work extraction efficiency of the turbine. Lower work extraction from the fluid results from a higher pressure loss due to an unfavorable shape of the vane. Additionally, the shape impacts the amount of heat transfer from the hot gas to the vane surface, hence, determining the cooling fluid requirements for the vane [3]. An optimally designed vane can lead to notable fuel and repair cost savings and increased longevity of the vane. The reference (baseline) shape for the nozzle guide vane used for the shape optimization is designed by researchers at the Von Karman Institute (VKI) [35].

2.1 Flow physics

Understanding the physics of the flow over the turbine vane is crucial for constructing the optimization problem.

In a gas turbine engine, gases exiting from the combustion chamber impinge on a circular cascade of nozzle guide vanes. High temperature and high pressure subsonic flow hits the leading edge of each vane and then accelerates over the suction side, reaching close to Mach one near the trailing edge on the suction side

of the vane where the boundary layer transitions from laminar to turbulent. In contrast, on the pressure side, the boundary layer stays laminar. The boundary layers after separation from the surface of the vane, merge into a turbulent wake. The exit pressure in gas turbine engines is much larger than 1 atm.

In the experimental setup of the VKI vane, the circular cascade is approximated as a linear cascade. The Reynolds number of the flow, computed using the chord length of the vane, is approximately 1,000,000. The downstream isentropic Mach number is 0.92. The chord length of the vane is $c_l = 67.6 \text{ mm}$. The Reynolds number is defined using the chord length of the vane and the density, velocity and viscosity of the inflow. Gourdain [14] and Morata [13] performed large eddy simulations of this flow problem at various Reynolds numbers.

The boundary layer development on the two sides of the vane and turbulent mixing in the wake lead to substantial drop in the stagnation pressure of the fluid. These phenomena discourage the use of blunt trailing edge for the vane as they can lead to earlier separation and higher pressure loss. There is a large increase in the heat transfer coefficient on the suction side due to the transition of the boundary layer from laminar to turbulent. This behavior rules out the use of sharp trailing edge for the vane as the material of the vane cannot simultaneously sustain high temperatures and high stress for prolonged time periods. The thickness, development and separation location of the boundary layers and the characteristics of the turbulent wake are greatly influenced by the shape of the vane near the trailing edge. Hence, the design optimization restricts shape parameterization of the vane to the trailing edge in order to lower the dimension of the design search space and maintain the enhancement potential of the candidate designs.

2.2 Numerical setup

Turbulent fluid flow is modeled using the compressible Navier-Stokes equations with the ideal gas law serving as an approximation to the thermodynamic state

equation [36]. The gas is assumed to be air.

$$\begin{aligned}
& \text{In } \mathbf{x} \in V, t \in [0, T], \\
& \frac{\partial \rho}{\partial t} + \nabla \cdot (\rho \mathbf{u}) = s_\rho \\
& \frac{\partial(\rho \mathbf{u})}{\partial t} + \nabla \cdot (\rho \mathbf{u} \mathbf{u}) + \nabla p = \nabla \cdot \sigma + \mathbf{s}_{\rho \mathbf{u}} \\
& \frac{\partial(\rho E)}{\partial t} + \nabla \cdot (\rho E \mathbf{u} + p \mathbf{u}) = \nabla \cdot (\mathbf{u} \cdot \sigma + \alpha \rho \gamma \nabla e) + s_{\rho E} \\
& \sigma = \mu(\nabla \mathbf{u} + \nabla \mathbf{u}^T) - \frac{2\mu}{3}(\nabla \cdot \mathbf{u})\mathbf{I} \\
& p = (\gamma - 1)\rho e \\
& e = E - \frac{\mathbf{u} \cdot \mathbf{u}}{2} \\
& c = \sqrt{\frac{\gamma P}{\rho}}
\end{aligned} \tag{1}$$

where V is the domain of the flow problem, T is the terminal time of the flow problem (which can be ∞), ρ is the density, \mathbf{u} is the velocity vector, ρE is the total energy, p is pressure, e is internal energy of the fluid, c is the speed of sound, γ is the isentropic expansion factor (for air $\gamma = 1.4$), μ is the viscosity field modeled using Sutherland's law for air

$$\mu = \frac{C_s T^{3/2}}{T + T_s} \tag{2}$$

where $T_s = 110.4 K$ and $C_s = 1.458 \times 10^{-6} \frac{kg}{m s \sqrt{K}}$. α is the thermal diffusivity modeled using

$$\alpha = \frac{\mu}{\rho Pr} \tag{3}$$

where Pr is the Prandtl number (for air $Pr = 0.71$). $s_\rho, \mathbf{s}_{\rho \mathbf{u}}, s_{\rho E}$ denote the source terms prescribed in a flow problem. In addition to the above equations, depending on the specifics of the flow problem, boundary conditions are prescribed on each of the boundary regions of the domain (S). Lastly, appropriate initial conditions for the flow variables, $\rho, \rho \mathbf{u}, \rho E$, are defined. the following reference quantities are defined for the flow problem

$$\begin{aligned}
\rho_r &= 1 \text{ kg/m}^3 \\
u_r &= 100 \text{ m/s} \\
p_r &= C_r \rho_r u_r^2 \\
\mu_r &= 1.8 \times 10^{-5} \text{ m}^2/\text{s}
\end{aligned} \tag{4}$$

where $C_r = 10.1325$ is a fixed constant.

The numerical approximation to the flow solution is obtained using large eddy simulations on a discretized domain of the 3-dimensional flow problem,

generally known as a mesh or a grid. In an LES, the large scale eddies of the flow are resolved by the grid while the contribution of the small scale eddies to the filtered Navier-Stokes equations are modeled using a sub-grid scale Reynolds stress model [36]. The choice of the LES model can have a large impact on the accuracy of the relevant statistical quantities of interest of the flow. In this paper, implicit LES model is used. In this model, the numerical error of the discretization scheme serves as the LES model. It has been shown that when using a dissipative discretization method, the numerical viscosity from the grid can be of the same order of magnitude as the sub-grid scale viscosity [37]. Hence, using an explicit LES model may be unnecessary.

The numerical solution of the flow problem is obtained on an unstructured hexahedral mesh using a second order finite volume method (FVM) [38]. The central differencing scheme is used to interpolate cell averages of the flow solution onto faces of the mesh [39]. The numerical fluxes for the conservative flow variables are computed using the Roe approximate Riemann solver [40]. An explicit time integration scheme, the strong stability preserving third order Runge-Kutta method [41], is used for time marching the numerical flow solution. The size of the time step is determined using the acoustic Courant-Friedrichs-Lewy (CFL) condition [42]. The flow solver is implemented in Python using a library, *adFVM* [43], that provides a high-level abstract application programming interface for writing efficient CFD applications. The flow solver is parallelized using the Message Passing Interface (MPI) library. The adjoint flow solver is implemented as a discrete adjoint solver using the Python library *adFVM* with the help of automatic differentiation. The checkpointing method [44] is used to reduce memory usage. The viscosity-stabilized adjoint method, described in Section 3, is implemented for the adjoint flow solver using an Euler-RK implicit-explicit time stepping scheme [45].

A 2-dimensional slice of the computational domain used to model the flow problem is shown in Figure 1. The x -direction is the direction of the inflow, the y -direction is the direction of the periodic cascade from the bottom to the top surface and the z -direction is perpendicular to the x and y -directions. The tip of the leading edge serves as the origin of the computational domain. Periodic boundary conditions are used in directions transverse to the flow direction. Static pressure equal to $1 atm$ is prescribed on the outlet boundary. A non-reflecting characteristic boundary condition is used on the inlet boundary of the domain [46]. The stagnation pressure (computed from the downstream isentropic Mach number) and stagnation temperature ($420 K$) are prescribed on the inlet boundary. Using this information on one side of the boundary and the solution fields from the interior of the domain on the other side, the Roe approximate Riemann solver is used to propagate the fluxes on the inlet boundary. The surface of the vane is maintained at a constant temperature of $300 K$. The span-wise extent is approximately $0.16 c_l$, which is sufficient to accurately capture most of the important flow features [14]. In order to resolve the small scale eddies of the flow near the wall, the dimensionless wall normal cell spacing (y_+) needs to be below 1 wall unit [47]. However, this paper does not adopt this practice due to computational cost considerations. As the

Reynolds number of the flow is high, the y_+ restriction along with a maximum CFL number of 1.2 over the domain of the flow problem, significantly lowers the maximum time step size that can be used by an explicit time integration scheme. To obtain results from the flow simulation in a reasonable time frame, the maximum y^+ is kept at 10. This does not appear to lead to significant loss in physical accuracy of the simulation as demonstrated by the comparison of the experimental heat transfer and static pressure data, obtained by Arts [35], with numerical data generated by an LES on an under resolved wall grid in Figures 2 and 3. The LES on the under resolved wall grid appears to provide better results than the LES on a resolved wall grid. This potentially can be attributed to the difference in sub-grid scale models, the former uses an implicit LES model while the latter uses the Wall-Adapting Local Eddy Viscosity (WALE) model which could be introducing modelling error in the solution. The maximum x^+ is 250 and maximum z^+ is 50. The total number of cells in the mesh of the computational domain is approximately 16 million. A visualization of the magnitude of an instantaneous velocity field of the flow over the turbine vane near the trailing edge is shown in Figure 4.

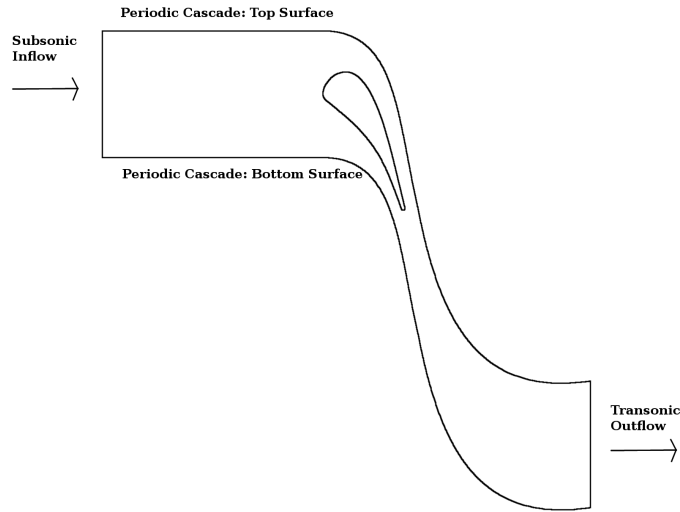


Figure 1: Turbine vane computational domain

2.3 Design objective

The design objective for the trailing edge shape optimization is a linear combination of the stagnation pressure loss downstream of the vane and heat transfer near the trailing edge of the vane. The stagnation pressure loss is represented by the infinite time-averaged and mass flow-averaged stagnation pressure loss

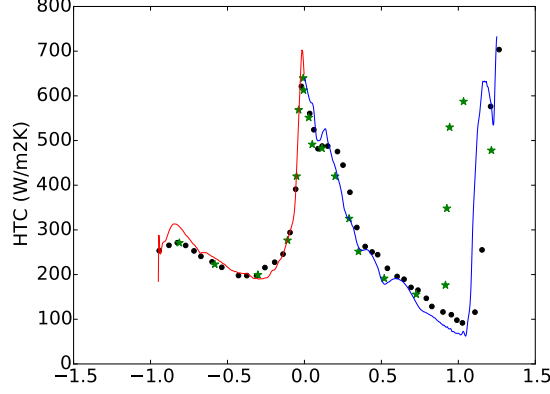


Figure 2: Comparison of heat transfer coefficient on the surface of the vane obtained from experimental data produced by Arts [35] (denoted by black dots), numerical data from an LES on a resolved wall grid produced by Gourdain [14] (denoted by green colored stars) and numerical data generated by an LES on an under-resolved wall grid (denoted by blue and red colored lines) at isentropic Mach number 0.9 and Reynolds number 10^6 . In the figure, the color blue denotes suction side, the color red denotes pressure side. The x -axis represents the distance from the leading edge along the surface of the vane normalized by the chord length.

coefficient (\bar{p}_l)

$$\bar{p}_l = \frac{\bar{p}_{t,l}}{p_{t,in}}$$

$$\bar{p}_{t,l} = \lim_{t_e \rightarrow \infty} \frac{1}{t_e} \int_0^{t_e} \frac{\int_{S_p} \rho_p u_n (p_{t,in} - p_{t,p}) dS_p}{\int_{S_p} \rho_p u_n dS_p} dt \quad (5)$$

$$p_{t,p} = p_p \left(1 + \frac{\gamma - 1}{2} M_p^2\right)^{\frac{\gamma}{\gamma - 1}}$$

$$p_{t,in} = p_{ex} \left(1 + \frac{\gamma - 1}{2} M_{is}^2\right)^{\frac{\gamma}{\gamma - 1}}$$

where M_p is the Mach number on the plane, p_p , ρ_p , $p_{t,p}$ are the pressure, density and stagnation pressure on the plane respectively, S_p represents the plane surface, u_n is the velocity normal to the plane surface, $p_{t,in}$ is the inlet stagnation pressure, p_{ex} is the exit static pressure and M_{is} is the downstream isentropic Mach number. A visualization of the time history of the instantaneous pressure loss is shown in Figure 5. The heat transfer is represented by the Nusselt number (Nu).

$$Nu = \frac{\bar{h}L}{k} \quad (6)$$

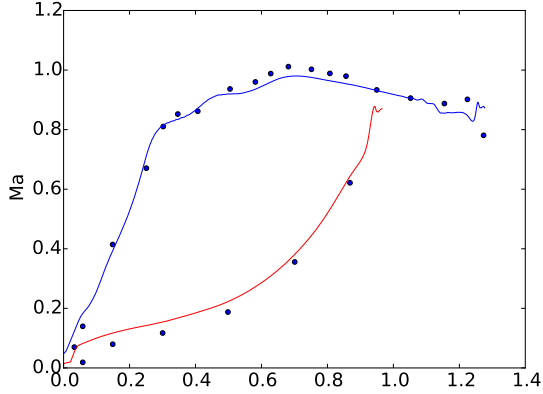


Figure 3: Comparison of isentropic Mach number on the surface of the vane obtained from experimental data produced by Arts [35] (denoted by blue dots) and numerical data generated by an LES on an under-resolved wall grid (denoted by blue and red colored lines) at isentropic Mach number 0.875 and Reynolds number 10^6 . In the figure, the color blue denotes suction side, the color red denotes pressure side. The x -axis represents the distance from the leading edge along the surface of the vane normalized by the chord length.

where k is the thermal conductivity at $T = 300\text{ K}$, $k = 0.028 \frac{\text{W}}{\text{mK}}$, L is the trailing edge radius for the baseline case, $0.0105 c_l$, and \bar{h} is the time-averaged heat transfer coefficient over a part of the vane starting from $0.414 c_l$ downstream of the leading edge in the direction of the inflow and leading up to the tip of the trailing edge. The equation for \bar{h} is

$$\bar{h} = \lim_{t_e \rightarrow \infty} \frac{1}{S_v t_e \Delta T} \int_0^{t_e} \int_{S_v} k \frac{\partial T}{\partial n} dS_v dt, \quad (7)$$

where S_v is the surface area and $\Delta T = 120\text{ K}$ is the temperature difference between the surface of the blade and the stagnation temperature of the flow. A visualization of the time history of the instantaneous heat transfer is shown in Figure 6. The design objective for the optimization is a linear combination of two quantities, the Nusselt number and pressure loss coefficient, and is given by

$$\bar{J} = a(Nu) + b(\bar{p}_l) \quad (8)$$

where $a = 5 \times 10^{-4}$ and $b = 0.4$. The values for a and b are chosen such that the contribution of both Nu and \bar{p}_l to the sum is equal for the baseline case.

As the fluid flow solution is obtained for a finite time, the infinite time-averages in Equations 5 and 7 are approximated using a finite time-average. The length of the time averaging interval is chosen to provide a statistically converged estimate of the infinite time average. A converged estimate is an

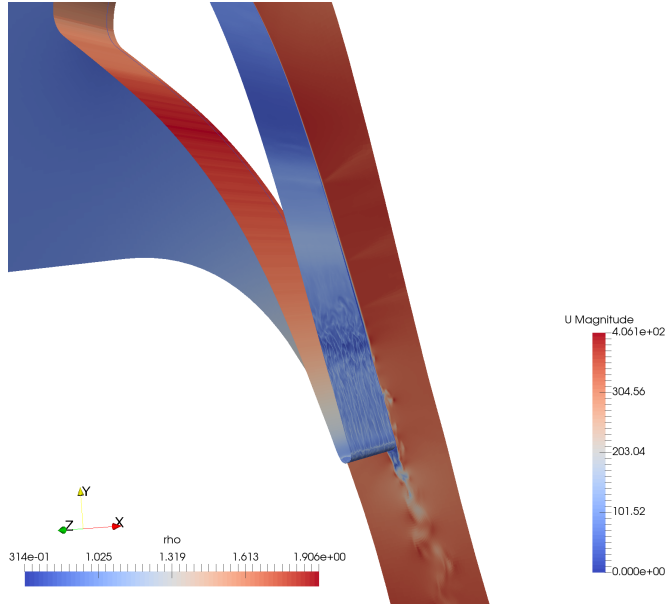


Figure 4: An instantaneous snapshot of the flow field near the trailing edge of the vane. The density (units: kg/m^3) is colored over the surface of the vane and the magnitude of the velocity field (units: m/s) is colored on the planar cross section.

estimate that has a standard deviation (or standard error) that is less than 10% of the magnitude of the estimate itself. Through a numerical investigation it is found to be equal to $N = 6$ time units. 1 time unit (t_r) is the time the flow takes to travel from the inlet boundary to the outlet boundary.

$$t_r = \frac{1.5c_l}{u_r} \quad (9)$$

This interval is sufficient to obtain the design objective with approximately 5% standard error relative to the estimate.

A procedure is required to compute an estimate for the finite time-average from an instantaneous time history of the design objective. The finite time-average can be modeled as a random variable. The mean estimate of this random variable can be computed using a sample average, \tilde{J}_N .

$$\tilde{J}_N = \frac{1}{N} \sum_{n=N_0}^N J_n \quad (10)$$

where J_n represents the instantaneous design objective at time step n . The time averaging is started after an initial transition period to allow for any transient effects in the time history to settle down into a statistical steady state.

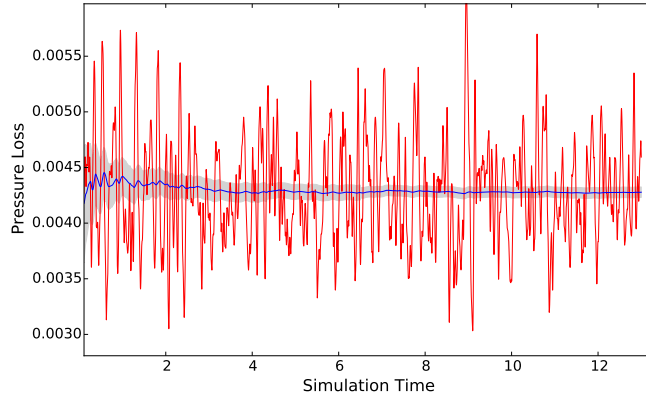


Figure 5: Scaled instantaneous pressure loss coefficient ($b(\bar{p}_i)$) plotted as a function of time (represented by time units). The blue time series denotes the cumulative mean and the gray shaded area denotes a single standard deviation of the sample mean. The procedure for time averaging is discussed in Section 2.3.

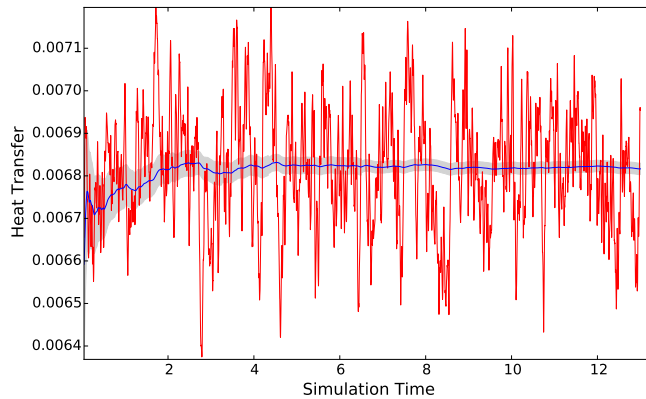


Figure 6: Scaled instantaneous Nusselt number ($a(Nu)$) plotted as a function of time (represented by time units). The blue time series denotes the cumulative mean and the gray shaded area denotes a single standard deviation of the sample mean. The procedure for time averaging is discussed in Section 2.3.

The transition period is determined by finding the time it takes for a running time-average to lie within 1 standard deviation of the full interval time-average. For the design objective of the trailing edge shape optimization problem, this period is approximately $N_0 = 1$ time units. It is large enough to encompass the

transition period for different trailing edge shapes.

The standard deviation of the mean estimate (or sample mean) provides an indication of the amount of error in the finite time-average approximation of the design objective. The standard statistical formula for computing the standard error of a sample mean cannot be used as the instantaneous values of the design objective are not independent and form a correlated time series. Oliver (2014) [48] suggested using data fitted autoregressive models to get the correlation function for the time series. This approach is adopted in this paper. Autoregressive models can be written in the following form

$$J_n = \sum_{i=1}^p a_i J_{n-i} + \epsilon_n \quad (11)$$

where a_i are the constant coefficients of the autoregressive model, p is the order of the model and ϵ_n are independent, identically distributed normal random variables, $\epsilon_n \sim N(0, \sigma^2)$. The coefficients of the model are determined using the Burg estimation algorithm with the *CIC* criterion to decide the model order [49]. Even though the actual model for the time series may not belong to the class of linear stochastic models, the variance computed using the model's correlation function can be utilized to provide a reasonable estimate of the variance of the sample mean.

$$Var(\tilde{J}_N) \approx \frac{Var(J_n)}{N_d} \quad (12)$$

$$N_d = \frac{N}{1 + 2 \sum_{k=1}^{\infty} \rho(k)} \quad (13)$$

where $\rho(k)$ is the autocorrelation between k time steps and N_d is the effective sample size.

2.4 Design parameterization

Parameterizing the trailing edge of the turbine vane is a challenging task. For the shapes to be valid, they have to satisfy a convexity condition about the chord line. Such a condition is required in order to ensure that there are no undulations or obstructions in the surface of the vane which can increase flow instability or cause back flow. The convexity condition imposes a nonlinear constraint on the shape parameters, increasing the complexity of the design optimization problem.

One way to get around the nonlinear constraint is to parameterize the trailing edge of a 2-dimensional turbine vane as a linear combination of 5 trailing edge shapes, with the weights serving as the parameters. If the candidate trailing edge shapes are convex, then they form a reduced basis of all convex shapes [50], ensuring that the parameterized trailing edge shape is convex. The linear combination is implemented as a weighted average of the 2-dimensional coordinates of the basis shapes. If the coordinates of the basis shape j are denoted by

x_i^j , then the coordinates of a new shape are given by

$$x_i(\boldsymbol{\alpha}) = \sum_{j=1}^5 \alpha_j x_i^j \quad (14)$$

The sum of the weights (α_j) is equal to 1. Hence, the weights α_j of the 5 basis shapes satisfy the following constraint,

$$\sum_{j=1}^5 \alpha_j = 1 \quad (15)$$

The above equality constraint can be transformed into an inequality constraint by eliminating one of the α_j variables. This results in a formation of a 4-dimensional parameterization of the trailing edge shape with the following inequality constraint,

$$\sum_{j=1}^4 \alpha_j \leq 1 \quad (16)$$

The 5 basis shapes are chosen such that the parameterized shapes explore a large subset of convex shapes. They are shown in Figure 7. One of the basis shapes is from the baseline turbine vane design from VKI. The 5 basis shapes are linearly independent, meaning that there are no two sets of parameters $\boldsymbol{\alpha}$ that generate the same shape.

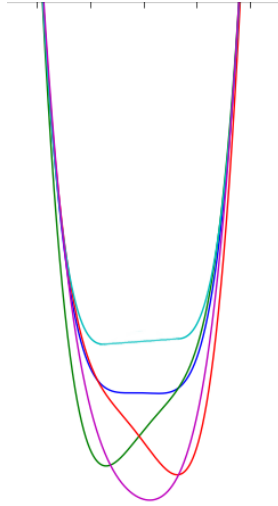


Figure 7: Visualization of the 5 basis shapes

Evaluating the design objective and gradient for a trailing edge shape requires the generation of a new mesh for obtaining the flow and adjoint solutions.

The mesh corresponding to the parameterized shape is formed by perturbing the mesh of the baseline design. The mesh generation process starts by projecting the nodes of the mesh of the baseline design onto the parameterized design by minimizing distance between the nodes of the respective designs. Once projected, a displacement vector is computed from the nodes of the baseline mesh nodes on the surface of the vane to parameterized mesh nodes. This displacement vector on the vane surface is propagated through the remaining mesh using a linear elasticity model for the mesh nodes [51, 52]. This model can be used under the assumption that the magnitude of the displacement vector is small. The linear elasticity equations are

$$\nabla \cdot \boldsymbol{\sigma} = 0 \quad (17)$$

$$\boldsymbol{\sigma} = \lambda \epsilon_{ii} \mathbf{I} + 2\mu \boldsymbol{\epsilon} \quad (18)$$

$$\boldsymbol{\epsilon} = \frac{1}{2}(\nabla \mathbf{u} + \nabla \mathbf{u}^T) \quad (19)$$

where \mathbf{u} is the displacement, λ and μ are constants which govern the elasticity of the mesh nodes for propagating the displacement. The linear elasticity equations are solved using the boundary condition $\mathbf{u} = \mathbf{c}$ for the mesh nodes on the surface of the vane, where \mathbf{c} is the displacement vector of the parameterized design from the baseline design.

The gradient for the new trailing edge shape is evaluated using the viscosity stabilized adjoint method, which is described in Section 3. The function that maps the parameters of the shape to the location of the parameterized mesh nodes is difficult to differentiate. Hence, instead of directly providing the gradient of the design objective with respect to the shape parameters, the adjoint method provides the gradient with respect to discrete mesh fields like cell centers, mesh normals, et cetera, which are typically used to represent the mesh in finite volume methods. These gradients are denoted by $\frac{\partial J}{\partial m_i}$. The finite difference method is used to obtain the gradient with respect to the parameters of the shape ($\frac{\partial J}{\partial \alpha_j}$).

$$\frac{\partial J}{\partial \alpha_j} \approx \frac{\partial J}{\partial m_i} \frac{(m_i(\boldsymbol{\alpha} + \boldsymbol{\epsilon}_j) - m_i(\boldsymbol{\alpha}))}{\epsilon} \quad (20)$$

where $\boldsymbol{\epsilon}_j$ is a zero vector with the same dimension as $\boldsymbol{\alpha}$ and with the j^{th} entry set to $\epsilon = 10^{-5}$. Hence, for each design objective gradient evaluation, a set of 4 meshes are generated by perturbing each shape parameter by ϵ separately. The corresponding perturbations in the discrete mesh fields for each of the shape parameters are utilized to obtain $\frac{(m_i(\boldsymbol{\alpha} + \boldsymbol{\epsilon}_j) - m_i(\boldsymbol{\alpha}))}{\epsilon}$. Multiplying this quantity with $\frac{\partial J}{\partial m_i}$ obtained from the adjoint method and summing over all the indices i provides the design objective gradient.

3 Adjoint-based design optimization

The adjoint method for physics-based numerical simulations is a widely used tool for accelerating the engineering design optimization process by efficiently

obtaining the gradient of the design objective function with respect to the design parameters. The adjoint method requires a single additional solution field (known as the adjoint solution) for computing the gradients, in comparison to the finite difference method of computing gradients which requires n additional solution fields for n design parameters [53].

3.1 Viscosity-stabilized adjoint method

Application of the adjoint method to LES produces large magnitude adjoint solutions which eliminates its effectiveness. This is especially true when the design objective is a long-time averaged quantity [21]. The divergence of the adjoint solution for turbulent fluid flows is explained by the chaotic dynamics of turbulence [54, 55]. Like many chaotic systems, turbulent flows exhibit the butterfly effect [56], which means that the instantaneous flow solution fields are sensitive to perturbations in the design parameters. The exponentially growing difference in the solution fields causes the adjoint method to incorrectly compute the gradients for long-time averaged quantities. The authors have proposed a solution to this problem by adding minimal amounts of localized artificial viscosity to the adjoint equations [26, 57] that is sufficient to stabilize the adjoint solution. Viscosity is added only in regions where there is a high likelihood of divergence of the adjoint flow field. Numerical results have shown that even with the artificial viscosity that stabilizes the adjoint solution, the accuracy of the gradients is maintained within 10-20% of the true design objective gradient.

The regions of divergence of the adjoint solution are found by performing an weighted L_2 norm or energy analysis of the Turkel symmetrized adjoint equations for compressible fluid flows [57]. An indicator field that shows the regions of divergence is given by the maximum generalized eigenvalue (λ_1) of $\frac{1}{2}(\mathbf{M} + \mathbf{M}^T)$ and \mathbf{N} where \mathbf{M} and \mathbf{N} are matrices defined at every point of the

domain of the flow problem and are given by

$$\begin{aligned}
\mathbf{M} &= \mathbf{M}_1 - \mathbf{M}_2 \\
\mathbf{M}_1 &= \frac{1}{2} \begin{pmatrix} \nabla \cdot u & \nabla_1 c & \nabla_2 c & \nabla_3 c & 0 \\ \nabla_1 c & \nabla \cdot u & 0 & 0 & 0 \\ \nabla_2 c & 0 & \nabla \cdot u & 0 & 0 \\ \nabla_3 c & 0 & 0 & \nabla \cdot u & 0 \\ 0 & 0 & 0 & 0 & T_r^2 \nabla \cdot u \end{pmatrix} \\
\mathbf{M}_2 &= \begin{pmatrix} \frac{\gamma-1}{2} \nabla \cdot u & \frac{1}{\rho c} \nabla_1 p & \frac{1}{\rho c} \nabla_2 p & \frac{1}{\rho c} \nabla_3 p & \frac{T_r^2}{2\rho c} \nabla \cdot u \\ \frac{\gamma-1}{2\rho c} \nabla_1 p & \nabla_1 u_1 & \nabla_2 u_1 & \nabla_3 u_1 & \frac{T_r^2}{2\gamma\rho\rho} \nabla_1 p \\ \frac{\gamma-1}{2\rho c} \nabla_2 p & \nabla_1 u_2 & \nabla_2 u_2 & \nabla_3 u_2 & \frac{T_r^2}{2\gamma\rho\rho} \nabla_2 p \\ \frac{\gamma-1}{2\rho c} \nabla_3 p & \nabla_1 u_3 & \nabla_2 u_3 & \nabla_3 u_3 & \frac{T_r^2}{2\gamma\rho\rho} \nabla_3 p \\ 0 & (\nabla_1 p - c^2 \nabla_1 \rho) & (\nabla_2 p - c^2 \nabla_2 \rho) & (\nabla_3 p - c^2 \nabla_3 \rho) & 0 \end{pmatrix} \\
\mathbf{N} &= \begin{pmatrix} 1 & 0 & 0 & 0 & 0 \\ 0 & 1 & 0 & 0 & 0 \\ 0 & 0 & 1 & 0 & 0 \\ 0 & 0 & 0 & 1 & 0 \\ 0 & 0 & 0 & 0 & T_r^2 \end{pmatrix}
\end{aligned} \tag{21}$$

where T_r is a dimensional constant quantity given by

$$T_r = C_t \frac{p_r}{u_r} \tag{22}$$

where C_t is a non-dimensional tunable factor that can be in the range $(0, \infty)$. For simplicity, C_t is set to 1. Figure 8 shows a visualization of the scalar field, λ_1 , for flow over a turbine vane. The scalar field is normalized by its spatial L_2 norm. The scalar field has a large magnitude in the trailing edge region of the suction side of the turbine vane. This is to be expected from a physical understanding of the problem as this is the region where the turbulent boundary layer is formed. The formation of a turbulent wake and flow separation leads to the divergence of the adjoint solution.

The adjoint solution is damped by adding artificial viscosity to the compressible adjoint equations. Viscosity is only added to the adjoint equations and not the original flow equations. The amount of viscosity added is proportional to λ_1 . The adjoint equations with the artificial viscosity are

$$-\frac{\partial \hat{\mathbf{w}}}{\partial t} - (\hat{\mathbf{A}}_i - \hat{\mathbf{A}}_i^v) \frac{\partial \hat{\mathbf{w}}}{\partial x_i} = \frac{\partial}{\partial x_i} (\hat{\mathbf{D}}_{ji}^T \frac{\partial \hat{\mathbf{w}}}{\partial x_j}) + \underbrace{\eta \frac{\mu_r}{\|\lambda_1\|_\infty \rho_r} \frac{\partial}{\partial x_i} (\lambda_1 \frac{\partial \hat{\mathbf{w}}}{\partial x_i})}_{\text{artificial viscosity term}} \tag{23}$$

where η is a tunable non-dimensional scaling factor, $\hat{\mathbf{w}}$ represents the adjoint solution and $\hat{\mathbf{A}}_i, \hat{\mathbf{A}}_i^v, \hat{\mathbf{D}}_{ji}$ represent linearized operators of the compressible Navier-Stokes equations.

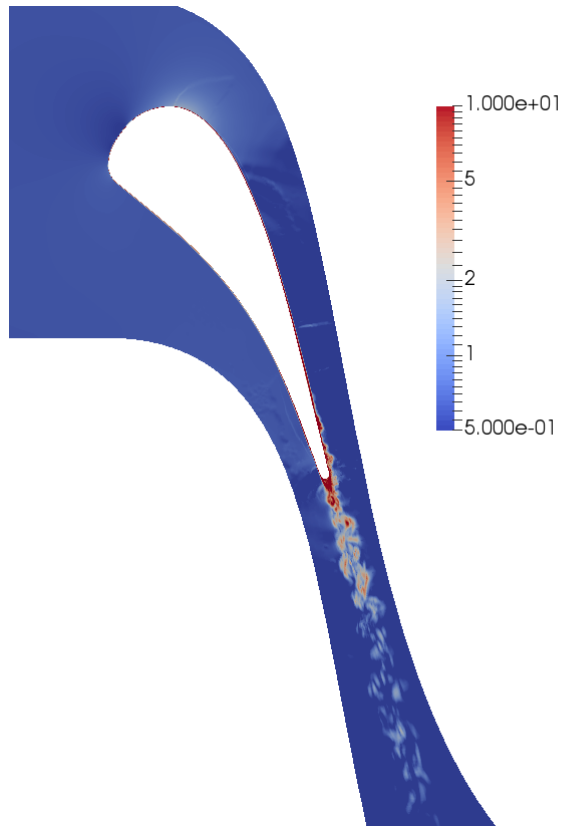


Figure 8: Visualization of the scalar field, λ_1

The choice of η is important. Too large values of η will result in fast stabilization of the adjoint solutions, but might adversely affect the accuracy of the gradients obtained from the adjoint solution. Too small values of η might not be sufficient to stabilize the adjoint solution. A reasonable strategy for deciding the appropriate value of η is to obtain multiple adjoint solutions with different values of η and choose the minimum η which stabilizes the adjoint solution over the entirety of the simulation. After obtaining multiple adjoint solutions with different values of the scaling factor, the optimal value of η for flow over the turbine vane is determined to be $\eta \approx 4,400$. The adjoint solution is obtained over a finite time interval whose length is 0.5 time units. This value is the minimum value of η for which the adjoint solution is stable for the baseline design of the trailing edge of the turbine vane. The value of η is kept constant for different parameterized designs of the trailing edge of the turbine vane. Empirically, it has been observed that the same value of η stabilizes the adjoint solution for different designs. Figure 9 shows the growth of adjoint energy for various artificial viscosity scaling factors ranging from $\eta = 0$ to $\eta \approx 13,000$.

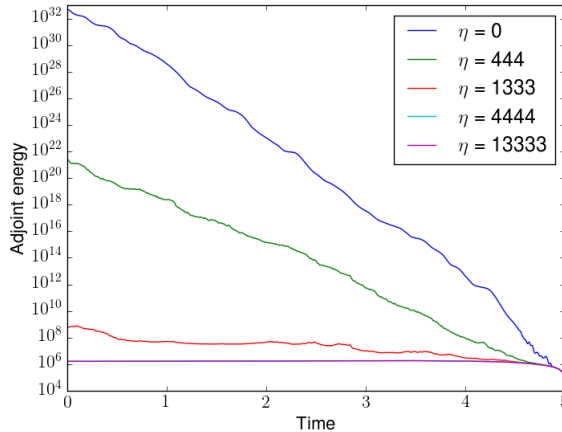


Figure 9: Plot showing the growth of adjoint energy (units: kg s/m^3) for various artificial viscosity scaling factors (η) as a function of time (represented by time units) for the turbine vane problem.

3.2 Optimization method

Design objectives in LES are often defined as infinite time averages. But, in practice, as the simulations are performed for a finite time, there is a sampling error associated with the objective function and gradient evaluations [58]. This error makes it difficult for the optimization algorithm to know whether a new design point with a lower objective value is actually better than the current optimal or if the difference can be attributed to noise. Additionally, the computational expense of LES mandates optimizers to utilize information from all previous evaluations to decide the next design point to evaluate and not just the last few design points. Bayesian optimization is a robust global optimization algorithm that is suitable for optimizing such noisy and expensive objective functions.

In this class of optimization algorithms, a surrogate model is fit to all the design evaluations using a Gaussian process [59]. The surrogate model explicitly models the amount of noise in the objective and gradient evaluations. It forms a global approximation of the design objective utilizing information from all past evaluations. In Bayesian optimization, the next design point to evaluate is decided by optimizing a metric which is a scalar function on the design space. The metric generally depends on the surrogate model and past evaluations. The Bayesian optimization loop begins by fitting the surrogate model to the past evaluations, proceeds to optimize the metric to find the next design point and finally evaluates the design. The loop terminates when there is no appreciable improvement in the design objective in consecutive evaluation or the computational resources to perform the optimization are exhausted. As the

evaluations are noisy, the optimal design at the end of the optimization process is the minimum of the surrogate model and not the design with the minimum objective value in all the evaluations.

Using a stochastic process to model the objective function helps in quantifying the uncertainty in a surrogate model that is trained on noisy evaluations. Additionally, it helps in designing a metric for deciding the next evaluation points that works towards finding the optimal design. A Gaussian process (GP) is a stochastic process whose mean ($\mu(\mathbf{x})$) and covariance functions ($k(\mathbf{x}, \mathbf{x}^*)$) are sufficient to completely define it, where \mathbf{x} is the point in the design space ω . A realization of a GP, evaluated on a set of discrete points \mathbf{X} , is a sample of a multivariate normal distribution with mean $\mu(\mathbf{X})$ and covariance $k(\mathbf{X}, \mathbf{X})$. If the design objective function is denoted by $f(x)$, then the corresponding GP is defined by [59]

$$\mu(\mathbf{x}) = \text{E}[f(\mathbf{x})], \quad (24)$$

$$k(\mathbf{x}, \mathbf{x}^*) = \text{E}[(f(\mathbf{x}) - \mu(\mathbf{x}))(f(\mathbf{x}^*) - \mu(\mathbf{x}^*))], \quad (25)$$

where the true functions $\mu(\mathbf{x})$ and $k(\mathbf{x}, \mathbf{x}^*)$ for the design objective are unknown. An initial estimate for the mean and covariance functions is known as the prior GP. On observing a few evaluations, the prior GP is updated using the Bayes rule to form the posterior GP. A prior mean function that is commonly used is $\mu(\mathbf{x}) = \mu_f$, where μ_f is a constant. The choice of the prior covariance function restricts the function space associated with the GP. As a majority of the design objectives typically observed in CFD are smooth (continuous and infinitely differentiable), the squared exponential kernel ($k(\mathbf{x}, \mathbf{x}^*) = \sigma_k^2 e^{-\left(\frac{|\mathbf{x}-\mathbf{x}^*|}{c_l}\right)^2}$) is used as the covariance function. This kernel has a few hyperparameters that need to be decided before beginning the optimization process. The hyperparameter, c_l , is the length scale of the kernel that determines how fast the function changes over the design space. The hyperparameter, σ_k^2 , is the signal variance and it controls how much nearby points in the design space are correlated.

Assuming additive noise in the design evaluations, the equation for an objective function and gradient evaluation is written as

$$\mathbf{y} = \begin{pmatrix} f(\mathbf{x}) + \epsilon_1(\mathbf{x}) \\ f'(\mathbf{x}) + \epsilon_2(\mathbf{x}) \end{pmatrix} \quad (26)$$

where ϵ_1, ϵ_2 are random variables representing the noise in the objective function and gradient evaluations respectively. $\epsilon_1(\mathbf{x})$ and $\epsilon_2(\mathbf{x})$ are assumed to be independent normal random variables, $\epsilon_1(\mathbf{x}) = N(0, \sigma_1^2(\mathbf{x}))$ and $\epsilon_2(\mathbf{x}) = N(0, \sigma_2^2(\mathbf{x}))$, where σ_1^2 and σ_2^2 denote the variance and are a function of the design space. Independence of ϵ_1 from ϵ_2 can be explained from the observation that the artificial viscosity in adjoint equations decorrelates the time series of the gradient evaluations from the time series of the objective evaluations. Due to a lack of knowledge in the correlation structure of the gradient components, the noise terms in each of the components of the gradient evaluation are assumed to be independent. The noise in each design point evaluation is assumed

to be independent of other design points as the correlation between the error due to finite time-averaging of the design objectives for different points in design space is observed to be zero. This is due to the fact that the chaotic time series, formed by the instantaneous design objective evaluations, exponentially diverges from the time series of even neighboring design points. The variance of the noise term is modeled heteroskedastically, which means that the amount of noise in the evaluations is a function of the design point. The dependence of σ_1^2 and σ_2^2 on \mathbf{x} is not known beforehand. Hence, they are modeled as independent logarithmic (log) GPs. This ensures that the variance term remains positive [60]. $\sigma_1(\mathbf{x})$ is represented as

$$\log\left(\frac{\sigma_1^2}{\mu_{\sigma_1^2}}\right) \sim GP(0, k_1(\mathbf{x}, \mathbf{x}^*)) \quad (27)$$

where $k_1(\mathbf{x}, \mathbf{x}^*) = e^{-\frac{|\mathbf{x}-\mathbf{x}^*|^2}{c_i^2}}$, $\mu_{\sigma_1^2}$ is the prior mean for the log GP. A similar expression can be used to represent $\sigma_2(\mathbf{x})$.

Using the aforementioned noise model, evaluations of the objective function and gradient for the design points are used to update the GP using Bayes rule to form a posterior GP. Consider a set of sample points \mathbf{X}_s and the corresponding function and gradient evaluations \mathbf{y}_s . The mean ($\boldsymbol{\mu}_p$) and covariance ($\boldsymbol{\Sigma}_p$) of the posterior process, when evaluated on a set of evaluation points \mathbf{X} is given by

$$\begin{aligned} \boldsymbol{\mu}_p &= \mathbf{K}^T(\mathbf{K}_s + \boldsymbol{\Sigma}_s)^{-1}\mathbf{y}_s, \\ \boldsymbol{\Sigma}_p &= k(\mathbf{X}, \mathbf{X}) - \mathbf{K}_*^T(\mathbf{K}_s + \boldsymbol{\Sigma}_s)^{-1}\mathbf{K}_*, \end{aligned} \quad (28)$$

$$\begin{aligned} \mathbf{K}_s &= \begin{pmatrix} k(\mathbf{X}_s, \mathbf{X}_s) & k'(\mathbf{X}_s, \mathbf{X}_s)^T \\ k'(\mathbf{X}_s, \mathbf{X}_s) & k''(\mathbf{X}_s, \mathbf{X}_s) \end{pmatrix}, \mathbf{K} = \begin{pmatrix} k(\mathbf{X}, \mathbf{X}_s) \\ k'(\mathbf{X}, \mathbf{X}_s) \end{pmatrix}, \\ \boldsymbol{\Sigma}_s &= \begin{pmatrix} \text{diag}[\sigma_1^2(\mathbf{X}_s)] & 0 \\ 0 & \text{diag}[\sigma_2^2(\mathbf{X}_s)] \end{pmatrix}, \end{aligned} \quad (29)$$

where k' denotes the derivative of k with respect to the first argument, k'' denotes the Hessian of the derivatives with respect to the first and second arguments.

The variance estimate of the sample mean of the design objective and gradient evaluations, discussed in Section 2.3, is used to update the noise GPs $\sigma_1(x)$ and $\sigma_2(x)$ using an expression similar to (28) without the gradient evaluations.

Before starting the Bayesian optimization process, it is important to have a set of evaluations from which an initial surrogate model can be created [61]. This step, known as design of experiment (DoE), is also used to estimate the hyperparameters of the GP. The hyperparameters are estimated using maximum likelihood estimation [59]. The mean quantities, μ_f , $\mu_{\sigma_1^2}$ and $\mu_{\sigma_2^2}$, are estimated using a sample mean of the design and gradient evaluations and their variance estimates. The design points for the DoE are chosen from a random subset of

points at the corners of the 4-dimensional hypercube that contains the design space, midpoints of the edges of the hypercube and the centroid of the hypercube. The points which do not satisfy the constraints of the design optimization problem are omitted.

In the Bayesian optimization loop, after fitting the surrogate model to all the past objective function and gradient evaluations, a metric function is optimized to find the next design point to evaluate. The metric can be designed to achieve a certain set of optimization goals [62, 63, 64, 65, 66]. For example, a popular optimization strategy involves exploring the design space in the initial part of the optimization process in order to improve the quality of the surrogate and then exploiting the surrogate model by evaluating designs close to the minimum of the surrogate in order to find the optimal design. A metric that reflects this strategy is the expected improvement (EI) criterion [33]. It provides a good balance between exploration and exploitation. EI is defined by the following expression

$$\text{EI}(\mathbf{x}) = \text{E}[\max(f_{min} - f(\mathbf{x}), 0)], \quad (30)$$

where f_{min} is the current estimated minimum of the objective, $f_{min} = \min_{\mathbf{x} \in \omega} \mu(\mathbf{x})$. For GPs, EI has a compact analytical form obtained by integrating over the expectation [67]

$$\text{EI}(\mathbf{x}) = (f_{min} - \mu(\mathbf{x}))\Phi\left(\frac{f_{min} - \mu(\mathbf{x})}{\sigma(\mathbf{x})}\right) + \sigma(\mathbf{x})\phi\left(\frac{f_{min} - \mu(\mathbf{x})}{\sigma(\mathbf{x})}\right), \quad (31)$$

where ϕ is the standard normal density, Φ is the standard normal distribution function and $\mu(\mathbf{x})$ and $\sigma(\mathbf{x})$ are the mean and standard deviation of the GP. The point in the design space (\mathbf{x}_n), which maximizes EI, $\mathbf{x}_n = \text{argmax}_{\mathbf{x} \in \omega} \text{EI}(\mathbf{x})$, is chosen as the next design to evaluate.

If the evaluations of the objective function are not noisy, EI can be shown to converge to the global minimum [68] provided the objective function belongs to the class of functions that can be represented by the surrogate model. But, when the evaluations are noisy, there is no proof of convergence. Additionally, it has been observed that using the EI metric can cause the optimization process to get stuck in a local minimum[69]. The reason is that the optimizer spends too many evaluations exploiting the GP without doing enough exploration. One possible solution to this problem is to choose f_{min} in such a way that EI is biased towards exploration.

$$f_{min} = \min_{\mathbf{x} \in \omega} (\mu(\mathbf{x}) + \beta\sigma(\mathbf{x})) \quad (32)$$

Increasing β leads to a significant increase in f_{min} , and consequently EI, for regions of the design space where $\sigma(\mathbf{x})$ is high. Hence, due to the larger EI values in unexplored regions, higher β results in more exploration.

Numerical experiments show that for various values of β the Bayesian optimization algorithm, with the modified EI metric, converges to the global optimum for a range of noisy functions including the noisy Rastrigin and long-time

averaged quantities of chaotic systems like the Lorenz system. Figure 10 shows the performance of the exploration biased EI metric on 2-dimensional optimization for two parameter choices of ζ for the noisy Rastrigin function. The function is given by

$$J(\mathbf{x}) = -30 + x_1^2 + x_2^2 - 10[\cos(2\pi\zeta x_1) + \cos(2\pi\zeta x_2)] + \psi z \quad (33)$$

where z is the standard normal random variable. The global minimum of this function is at $\mathbf{x} = (0, 0)$ and the minimum objective value is -50 . ψ is set to 4, which means that the objective function has a large amount of noise. When ζ is set to 0.5, the objective function has a lower number of local minima than when $\zeta = 1.5$. Figure 10 shows the trajectory of the distance of the minimum evaluation design point from the global minimum design point, averaged over 1000 runs of the optimizer. For the objective function with $\zeta = 0.5$, using any positive value of β results in the Bayesian optimization algorithm finding an optimal design that is closer to the global minimum than using $\beta = 0$. Using higher values of β enables the optimizer to explore more and reach a lower objective value. For the objective function with $\zeta = 1.5$, using $\beta = 1, 2$ or 3 results in better performance for the Bayesian optimization algorithm. The high number of local minima lowers the convergence rate of the various optimization algorithms with different values of β and increases the difficulty of finding the global optimal design. Similar to the $\zeta = 0.5$ case, positive values of β causes the optimizer to suppress exploitation of local minima and do more exploration. For all the optimization runs, the number of DoE points are set to 4.

3.3 Algorithm

The final optimization procedure for the trailing edge shape optimization problem, where the number of parameters in the optimization problem is $n = 4$, is described below

1. Evaluate $2n$ design points, where the design points are obtained from a design of experiment.
2. Decide hyperparameters for GP using maximum likelihood estimation applied to the $2n$ design evaluations.
3. Obtain posterior GP by fitting the surrogate model to all the past design evaluations.
4. Find next design point to evaluate by maximizing the exploration biased EI metric using $\beta = 1$.
5. Evaluate design point.
6. If the computational resources are exhausted or the optimization process has reached convergence, then return the optimal design, else repeat the process starting from step 3.

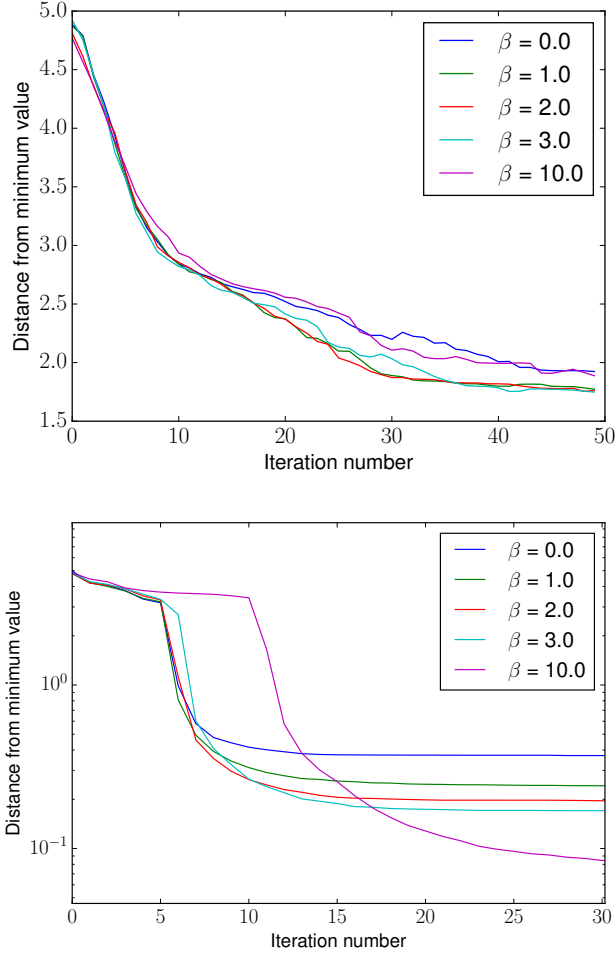


Figure 10: Comparison of the distance from the global minimum of the minimum design evaluated by the Bayesian optimization algorithm using different β values for the modified EI metric on the modified noisy Rastrigin function. Top figure: Rastrigin function with $\zeta = 1.5$. Bottom figure: Rastrigin function with $\zeta = 0.5$.

The cost of this algorithm is $(10n + 5m)C_p$, where m is the number of design evaluations in the optimization loop and C_p is the cost of obtaining the design objective value (or a single flow solution). The cost of a design evaluation is $5C_p$, as the typical cost of obtaining the design objective gradient (or a single adjoint solution) is $4C_p$.

4 Results

The shape of the trailing edge of the turbine vane is optimized using the modified Bayesian optimization algorithm utilizing the viscosity stabilized adjoint method for computing gradients. The optimization process begins with a design of experiment for 8 evaluations. The hyperparameters for the Gaussian process are $c_l = (0.7, 0.4, 0.5, 0.3)$ and $\sigma_k^2 = 10^{-6}$. The prior means for the GPs are $\mu_f = 0.0092$, $\mu_{\sigma_1^2} = 5 \times 10^{-9}$ and $\mu_{\sigma_2^2} = (10^{-9}, 10^{-7}, 10^{-8}, 10^{-7})$. The Bayesian optimizer is run for a total of 16 design objective and gradient evaluations. The value of β for the exploration biased EI metric is set to 1. During the optimization, multiple trailing edge shapes are found which have a lower design objective value. The optimization ends when consecutive designs evaluated by the optimizer do not lead to a reduction in the design objective value or its standard deviation. Figure 11 shows how the optimizer spends a majority of the initial evaluations on exploration (high standard deviation and high mean objective value of the posterior GP at evaluation point) and the evaluations towards the end of the optimization process in exploitation (low standard deviation and low mean objective value of the posterior GP at evaluation point).

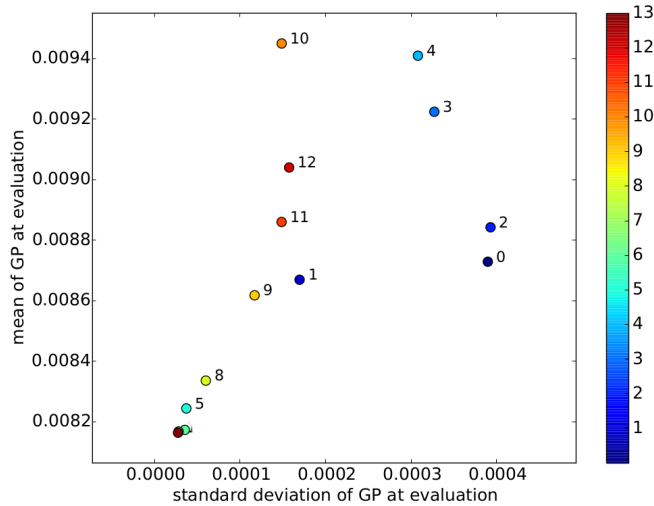


Figure 11: Plot of the design objective mean value and standard deviation of the posterior GP evaluated at the design point decided by the modified EI metric at each step of the optimization process. The points in the plot are colored and labeled by the optimization step number.

The optimization used a mixture of computational resources consisting of CPUs and GPUs. The design objective value was obtained by computing the numerical flow solution on an Nvidia GeForce GTX 1080Ti, which has 3584

CUDA cores and 11 GB RAM. The design objective gradient was obtained by computing the numerical adjoint solution on 16 Intel Xeon E5-1650 CPUs, where each of the CPUs has 4 cores and 32 GB RAM. The CPUs are interconnected using Gigabit Ethernet. The time to solution for a single design objective value is 12 hours and for a single design objective gradient is 12 hours. Hence, the total computational cost of the optimization is 18,432 CPU core hours and 288 GPU hours.

4.1 Comparison of optimal and baseline designs

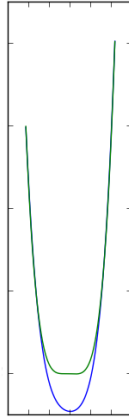


Figure 12: Visualization of the current optimal design (blue color) and baseline design (green color)

The optimal design at the end of the optimization process is shown in Figure 12. The baseline design has a design objective value equal to 0.00931 ± 0.0004 , whereas the optimal design has the objective value 0.008124 ± 0.00003 . The optimal design has an approximately 12% reduction in Nusselt number and 16% reduction in pressure loss coefficient. The design of experiment procedure produced a design with an objective value 0.00831. Consequently, the optimization procedure led to a 2.2% improvement in the design objective over the design of experiment.

A visualization of the magnitude of the instantaneous velocity field (U) and the gradient of the temperature field ($\text{grad}T$) are shown in Figure 13 and 14 respectively. A comparison of the two fields for the baseline and optimal design shows that the optimal design has a slightly thinner turbulent boundary layer on the suction side near the trailing edge. The width of the wake and the size of the vortex structures in the wake are smaller in the optimal design. Both these

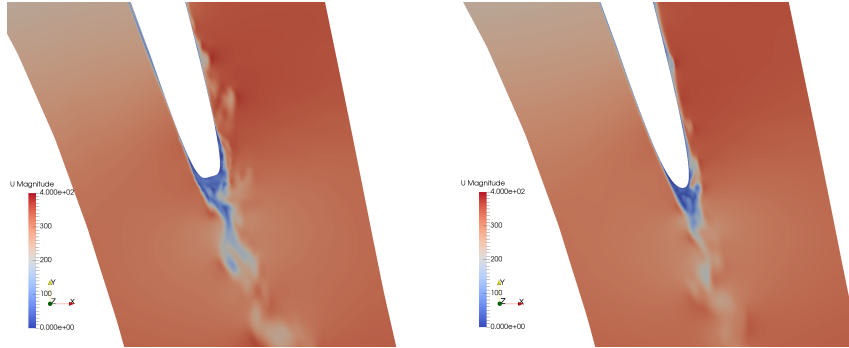


Figure 13: Left figure: Visualization of velocity field for baseline design. Right figure: Visualization of velocity field for optimal design

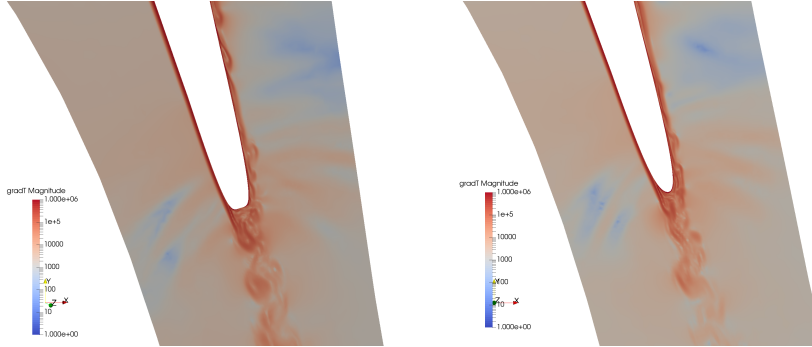


Figure 14: Left figure: Visualization of gradient of temperature field for baseline design. Right figure: Visualization of gradient of temperature field for current optimal design

factors contribute to the lower stagnation pressure loss in the optimal design. A thicker turbulent boundary layer leads to a higher convective heat transfer due to more mixing in the flow. Hence, the optimal design has a lower heat transfer than the baseline design. Finally, visualizations of the instantaneous design objective for the baseline and optimal designs are shown in Figure 15.

4.2 Comparison to Bayesian optimization without gradients

In order to quantify the utility of the gradient in the optimization process a comparison is performed between Bayesian optimization with and without gradients. Running a separate optimization without gradients is too expensive as this would involve running a large number of large eddy simulations. Hence, the two Bayesian optimization algorithms are compared by averaging multiple optimization runs that use an approximate LES design objective function. This

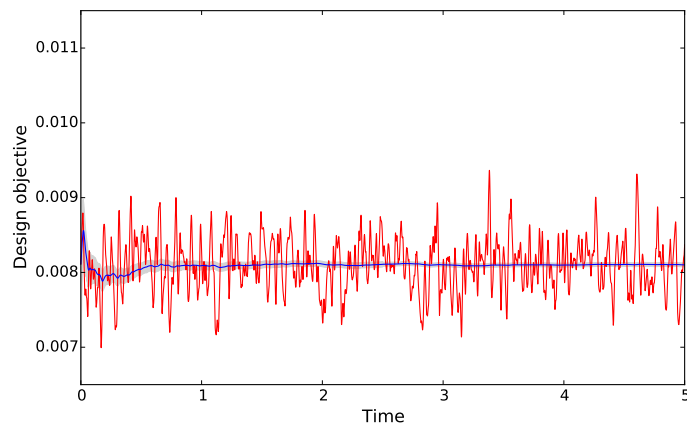
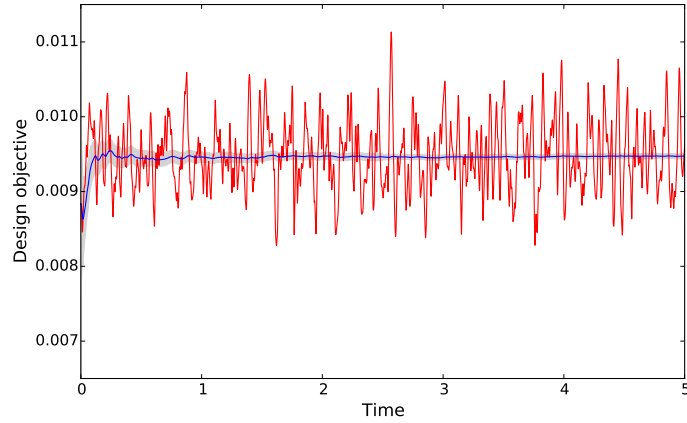


Figure 15: Top figure: Visualization of design objective for baseline design. Bottom figure: Visualization of design objective for current optimal design

objective is a Gaussian process which is trained on all the objective and gradient evaluations obtained during the adjoint-based design optimization process. Both the Bayesian optimization algorithms utilize the same DoE evaluations obtained during the adjoint-based design optimization. While running the optimizations, whenever the algorithm requires an evaluation for a particular design point, the objective is evaluated (including gradients if required) by sampling the Gaussian process at that point using Equation 26 by replacing $f(\boldsymbol{x})$ and $f'(\boldsymbol{x})$ with the mean of the corresponding Gaussian process. The noise term is realized by sampling the normal distribution with zero mean and variance computed from the mean of the noise log GP in accordance with Equation 27.

Figure 16 shows the trajectories of the minimum objective value for the two

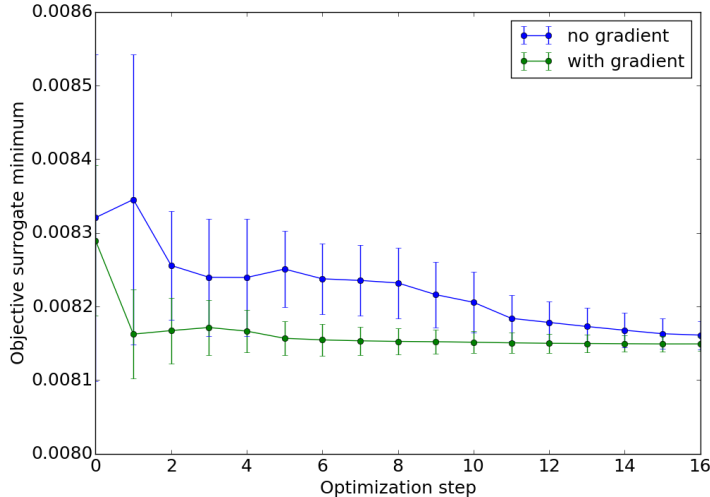


Figure 16: Comparison between Bayesian optimization with and without gradients

optimization algorithms as a function of the number of function evaluations. The minimum objective value as reported by the optimizers is minimum of the mean function of the posterior GP of the optimization algorithm. The figure shows a trajectory of the mean and the uncertainty corresponding to a single standard deviation of the posterior GP at the design point with the minimum objective value. The Bayesian optimizers with and without gradients are executed 1000 times to achieve a statistically converged Monte Carlo estimate of the optimization trajectory. The estimates provide less than 1% relative sample standard deviation for each mean value in the optimization trajectory.

From the figure it can be seen that the Bayesian optimization with gradients performs significantly better than optimizer without gradients as it reaches the optimal design faster. Furthermore, the optimizer with gradients obtains the minimum design objective value with a much lower standard deviation.

5 Conclusion

Adjoint-based design optimization using large eddy simulations is a powerful tool for design of turbomachinery components. Using a viscosity-stabilized adjoint method and a gradient utilizing Bayesian optimization method, the trailing edge of a gas turbine vane was optimized. The optimal design has a 12% reduction in Nusselt number and 16% reduction in pressure loss coefficient.

The Bayesian optimizer has a few issues scaling to a large number of design

parameters (> 20). Further research needs to be performed in order to either increase its efficiency for higher dimensional problems or investigate alternative optimization algorithms like multi-start stochastic gradient descent. The success of the adjoint-based design optimization method using LES increases its applicability to more challenging design problems like shape design of an entire low-pressure turbine blade.

6 Acknowledgements

The authors thank GE Aviation for providing funding and valuable feedback for this project. This paper uses results obtained from the Mira supercomputer of the Argonne Leadership Computing Facility, which is a DOE Office of Science User Facility supported under Contract DE-AC02-06CH11357.

References

- [1] Greitzer, E. M., Tan, C. S., and Graf, M. B., 2007. *Internal flow: concepts and applications*, Vol. 3. Cambridge University Press.
- [2] Talnikar, C., Blonigan, P., Bodart, J., and Wang, Q., 2014. “Parallel Optimization for LES”. In *Proceedings of the Summer Program*, p. 315.
- [3] Han, J.-C., Dutta, S., and Ekkad, S., 2012. *Gas turbine heat transfer and cooling technology*. CRC Press.
- [4] Pironneau, O., 1974. “On optimum design in fluid mechanics”. *Journal of Fluid Mechanics*, **64**(1), pp. 97–110.
- [5] Giles, M. B., and Pierce, N. A., 2000. “An introduction to the adjoint approach to design”. *Flow, turbulence and combustion*, **65**(3-4), pp. 393–415.
- [6] Marsden, A. L., Wang, M., Dennis, J., and Moin, P., 2007. “Trailing-edge noise reduction using derivative-free optimization and large-eddy simulation”. *Journal of Fluid Mechanics*, **572**, pp. 13–36.
- [7] Forrester, A. I., Bressloff, N. W., and Keane, A. J., 2006. “Optimization using surrogate models and partially converged computational fluid dynamics simulations”. *Proceedings of the Royal Society of London A: Mathematical, Physical and Engineering Sciences*, **462**(2071), pp. 2177–2204.
- [8] Campana, E. F., Peri, D., Tahara, Y., and Stern, F., 2006. “Shape optimization in ship hydrodynamics using computational fluid dynamics”. *Computer Methods in Applied Mechanics and Engineering*, **196**(1), pp. 634 – 651.
- [9] Jameson, A., 1995. “Optimum aerodynamic design using CFD and control theory”. *AIAA paper*, **1729**, pp. 124–131.

- [10] Economon, T. D., Palacios, F., and Alonso, J. J., 2013. “A viscous continuous adjoint approach for the design of rotating engineering applications”. *AIAA Paper*, **2580**, pp. 24–27.
- [11] Pironneau, O., et al., 1992. “Optimal Shape Design with Applications to Aerodynamics”. In *Shape Optimization and Free Boundaries*. Springer, pp. 211–251.
- [12] Lyu, Z., and Martins, J. R., 2014. “Aerodynamic design optimization studies of a blended-wing-body aircraft”. *Journal of Aircraft*, **51**(5), pp. 1604–1617.
- [13] Morata, E. C., Gourdain, N., Duchaine, F., and Gicquel, L., 2012. “Effects of free-stream turbulence on high pressure turbine blade heat transfer predicted by structured and unstructured LES”. *International Journal of Heat and Mass Transfer*, **55**(21), pp. 5754–5768.
- [14] Gourdain, N., Gicquel, L. Y., and Collado, E., 2012. “Comparison of RANS and LES for prediction of wall heat transfer in a highly loaded turbine guide vane”. *Journal of Propulsion and Power*, **28**(2), pp. 423–433.
- [15] Medic, G., Joo, J., Lele, S., and Sharma, O., 2012. “Prediction of heat transfer in a turbine cascade with high levels of free-stream turbulence”. In *Proceedings of the Summer Program*, p. 147.
- [16] Bhaskaran, R., and Lele, S. K., 2011. “Heat Transfer Prediction in High Pressure Turbine Cascade with Free-Stream Turbulence using LES”. *AIAA Paper*(2011-3266).
- [17] Kawai, S., and Lele, S. K., 2010. “Large-eddy simulation of jet mixing in supersonic crossflows”. *AIAA journal*, **48**(9), pp. 2063–2083.
- [18] Laskowski, G. M., Kopriva, J., Michelassi, V., Shankaran, S., Paliath, U., Bhaskaran, R., Wang, Q., Talnikar, C., Wang, Z. J., and Jia, F. *Future Directions of High Fidelity CFD for Aerothermal Turbomachinery Analysis and Design*.
- [19] Moin, P., and Kim, J., 1997. “Tackling turbulence with supercomputers”. *Scientific American*, **276**(1), pp. 46–52.
- [20] Wang, Q., and Gao, J.-H., 2013. “The drag-adjoint field of a circular cylinder wake at Reynolds numbers 20, 100 and 500”. *Journal of Fluid Mechanics*, **730**, pp. 145–161.
- [21] Blonigan, P., Chen, R., Wang, Q., and Larsson, J., 2012. “Towards adjoint sensitivity analysis of statistics in turbulent flow simulation”. In *Proceedings of the Stanford Center of Turbulence Research Summer Program 2014*, p. 229.

- [22] Blonigan, P., 2016. “Least Squares Shadowing for sensitivity analysis of large chaotic systems and fluid flows”. PhD thesis, Massachusetts Institute of Technology.
- [23] Chandramoorthy, N., Fernandez, P., Talnikar, C., and Wang, Q., 2019. “Feasibility Analysis of Ensemble Sensitivity Computation in Turbulent Flows”. *AIAA Journal*, **57**(10), pp. 4514–4526.
- [24] Ni, A., Wang, Q., Fernández, P., and Talnikar, C., 2019. “Sensitivity analysis on chaotic dynamical systems by Finite Difference Non-Intrusive Least Squares Shadowing (FD-NILSS)”. *Journal of Computational Physics*, **394**, pp. 615 – 631.
- [25] Ni, A., and Talnikar, C., 2019. “Adjoint sensitivity analysis on chaotic dynamical systems by Non-Intrusive Least Squares Adjoint Shadowing (NIL-SAS)”. *Journal of Computational Physics*, **395**, pp. 690 – 709.
- [26] Talnikar, C., Wang, Q., and Laskowski, G., 2016. “Unsteady adjoint of pressure loss for a fundamental transonic turbine vane”. *Journal of Turbomachinery*.
- [27] Talnikar, C. A., Blonigan, P. J., Bodart, J., and Wang, Q., 2015. “Optimization with LES–algorithms for dealing with sampling error of turbulence statistics”. In 53rd AIAA Aerospace Sciences Meeting, p. 1954.
- [28] Rios, L. M., and Sahinidis, N. V., 2013. “Derivative-free optimization: A review of algorithms and comparison of software implementations”. *J. Global Optim.*, **56**(3), pp. 1247–1293.
- [29] Robbins, H., and Monro, S., 1951. “A stochastic approximation method”. *The annals of mathematical statistics*, pp. 400–407.
- [30] Spall, J. C., 1992. “Multivariate stochastic approximation using a simultaneous perturbation gradient approximation”. *IEEE transactions on automatic control*, **37**(3), pp. 332–341.
- [31] Polyak, B. T., and Juditsky, A. B., 1992. “Acceleration of stochastic approximation by averaging”. *SIAM Journal on Control and Optimization*, **30**(4), pp. 838–855.
- [32] Huyer, W., and Neumaier, A., 2008. “SNOBFIT–stable noisy optimization by branch and fit”. *ACM Transactions on Mathematical Software (TOMS)*, **35**(2), p. 9.
- [33] Jones, D. R., Schonlau, M., and Welch, W. J., 1998. “Efficient global optimization of expensive black-box functions”. *J. Global Optim.*, **13**(4), pp. 455–492.
- [34] Wu, J., Poloczek, M., Wilson, A. G., and Frazier, P. I., 2017. “Bayesian Optimization with Gradients”. *arXiv preprint arXiv:1703.04389*.

- [35] Arts, T., and de Rouvroit, M. L., 1992. “Aero-thermal performance of a two-dimensional highly loaded transonic turbine nozzle guide vane: A test case for inviscid and viscous flow computations”. *J. Turbomach.*, **114**(1), pp. 147–154.
- [36] Garnier, E., Adams, N., and Sagaut, P., 2009. *Large eddy simulation for compressible flows*. Springer Science & Business Media.
- [37] Moeng, C.-H., and Wyngaard, J. C., 1989. “Evaluation of turbulent transport and dissipation closures in second-order modeling”. *Journal of the Atmospheric Sciences*, **46**(14), pp. 2311–2330.
- [38] LeVeque, R. J., 2002. *Finite volume methods for hyperbolic problems*, Vol. 31. Cambridge university press.
- [39] Versteeg, H., and Malalasekera, W., 1995. “An Introduction to Computational Fluid Dynamics”. *The finite volume method*.
- [40] Roe, P. L., 1981. “Approximate Riemann solvers, parameter vectors, and difference schemes”. *Journal of computational physics*, **43**(2), pp. 357–372.
- [41] Macdonald, C. B., 2003. “Constructing high-order Runge-Kutta methods with embedded strong-stability-preserving pairs”. PhD thesis, Simon Fraser University.
- [42] Courant, R., Friedrichs, K., and Lewy, H., 1967. “On the partial difference equations of mathematical physics”. *IBM journal of Research and Development*, **11**(2), pp. 215–234.
- [43] Talnikar, C., and Wang, Q., 2019. “A two-level computational graph method for the adjoint of a finite volume based compressible unsteady flow solver”. *Parallel Computing*, **81**, pp. 68–84.
- [44] Wang, Q., Moin, P., and Iaccarino, G., 2009. “Minimal repetition dynamic checkpointing algorithm for unsteady adjoint calculation”. *SIAM Journal on Scientific Computing*, **31**(4), pp. 2549–2567.
- [45] Ascher, U. M., Ruuth, S. J., and Spiteri, R. J., 1997. “Implicit-explicit Runge-Kutta methods for time-dependent partial differential equations”. *Applied Numerical Mathematics*, **25**(2-3), pp. 151–167.
- [46] Poinso, T. J., and Lele, S., 1992. “Boundary conditions for direct simulations of compressible viscous flows”. *Journal of computational physics*, **101**(1), pp. 104–129.
- [47] Choi, H., and Moin, P., 2012. “Grid-point requirements for large eddy simulation: Chapman’s estimates revisited”. *Physics of Fluids (1994-present)*, **24**(1), p. 011702.

- [48] Oliver, T. A., Malaya, N., Ulerich, R., and Moser, R. D., 2014. “Estimating uncertainties in statistics computed from direct numerical simulation”. *Physics of Fluids*, **26**(3), p. 035101.
- [49] Burg, J. P., Luenberger, D. G., and Wenger, D. L., 1982. “Estimation of structured covariance matrices”. *Proceedings of the IEEE*, **70**(9), pp. 963–974.
- [50] Samareh, J. A., 2001. “Survey of shape parameterization techniques for high-fidelity multidisciplinary shape optimization”. *AIAA journal*, **39**(5), pp. 877–884.
- [51] Sokolowski, J., and Zolésio, J.-P., 1992. “Introduction to shape optimization”. In *Introduction to Shape Optimization*. Springer, pp. 5–12.
- [52] Dwight, R. P., 2009. “Robust mesh deformation using the linear elasticity equations”. *Computational Fluid Dynamics 2006*, pp. 401–406.
- [53] Giles, M. B., and Pierce, N. A., 1997. “Adjoint equations in CFD: duality, boundary conditions and solution behaviour”. *AIAA paper*, **1850**, p. 1997.
- [54] Lapeyre, G., 2002. “Characterization of finite-time Lyapunov exponents and vectors in two-dimensional turbulence”. *Chaos: An Interdisciplinary Journal of Nonlinear Science*, **12**(3), pp. 688–698.
- [55] Maurer, J., and Libchaber, A., 1980. “Effect of the Prandtl number on the onset of turbulence in liquid 4He”. *Journal de Physique lettres*, **41**(21), pp. 515–518.
- [56] Strogatz, S. H., 2014. *Nonlinear dynamics and chaos: with applications to physics, biology, chemistry, and engineering*. Westview press.
- [57] Talnikar, C., 2018. “Viscosity stabilized adjoint method for unsteady compressible Navier-Stokes equations”. PhD thesis, Massachusetts Institute of Technology.
- [58] Oliver, T., Malaya, N., Ulerich, R., and Moser, R., 2014. “Estimating uncertainties in statistics computed from direct numerical simulation”. *Phys. Fluids*, **26**.
- [59] Rasmussen, C., and Williams, C., 2006. *Gaussian Processes for Machine Learning*. MIT Press.
- [60] Kersting, K., Plagemann, C., Pfaff, P., and Burgard, W., 2007. “Most likely heteroscedastic Gaussian process regression”. In Proceedings of the 24th international conference on Machine learning, ACM, pp. 393–400.
- [61] Pronzato, L., and Müller, W. G., 2012. “Design of computer experiments: space filling and beyond”. *Statistics and Computing*, **22**(3), pp. 681–701.

- [62] Ginsbourger, D., Le Riche, R., Carraro, L., et al., 2009. “A multi-points criterion for deterministic parallel global optimization based on Gaussian processes”. *J. Global Optim., in revision*.
- [63] Contal, E., Buffoni, D., Robicquet, A., and Vayatis, N., 2013. “Parallel Gaussian process optimization with upper confidence bound and pure exploration”. In *Joint European Conference on Machine Learning and Knowledge Discovery in Databases*, Springer, pp. 225–240.
- [64] Swersky, K., Snoek, J., and Adams, R. P., 2014. “Freeze-thaw Bayesian optimization”. *arXiv preprint arXiv:1406.3896*.
- [65] Picheny, V., Ginsbourger, D., Richet, Y., and Caplin, G., 2013. “Quantile-based optimization of noisy computer experiments with tunable precision”. *Technometrics*, **55**(1), pp. 2–13.
- [66] Hennig, P., and Schuler, C. J., 2012. “Entropy search for information-efficient global optimization”. *Journal of Machine Learning Research*, **13**(Jun), pp. 1809–1837.
- [67] Snoek, J., Larochelle, H., and Adams, R. P., 2012. “Practical Bayesian optimization of machine learning algorithms”. In *Adv. Neur. In.*, pp. 2951–2959.
- [68] Vazquez, E., and Bect, J., 2010. “Convergence properties of the expected improvement algorithm with fixed mean and covariance functions”. *Journal of Statistical Planning and inference*, **140**(11), pp. 3088–3095.
- [69] Picheny, V., Ginsbourger, D., and Richet, Y., 2010. “Noisy expected improvement and on-line computation time allocation for the optimization of simulators with tunable fidelity”.